Soft Matter

Accepted Manuscript

This is an *Accepted Manuscript*, which has been through the Royal Society of Chemistry peer review process and has been accepted for publication.

Accepted Manuscripts are published online shortly after acceptance, before technical editing, formatting and proof reading. Using this free service, authors can make their results available to the community, in citable form, before we publish the edited article. We will replace this *Accepted Manuscript* with the edited and formatted *Advance Article* as soon as it is available.

You can find more information about *Accepted Manuscripts* in the Information for Authors.

Please note that technical editing may introduce minor changes to the text and/or graphics, which may alter content. The journal's standard Terms & Conditions and the Ethical guidelines still apply. In no event shall the Royal Society of Chemistry be held responsible for any errors or omissions in this *Accepted Manuscript* or any consequences arising from the use of any information it contains.

ROYAL SOCIETY OF CHEMISTRY

www.rsc.org/softmatter

ARTICLE TYPE www. rsc.org/xxxxxx | XXXXXXXX

Pinning and wicking in regular pillar arrays

Ciro Semprebon*[a], Pontus Forsberg[b,c], Craig Priest[b], and Martin Brinkmann[a,d]

Received Xth XXXXXXXXXX 20XX, Accepted Xth XXXXXXXXX 20XX
First published on the web Xth XXXXXXXXXX 200X
DOI: 10.1039/b000000x

Pinning of a liquid meniscus wicking a square array of pillars is investigated in numerical energy minimzations and compared to wetting experiments. Our combined study shows that criteria for spontaneous film formation based on thermodynamic considerations as well as on simple geometric modelling of the meniscus shape are insufficient to predict the onset of wicking. High aspect ratio pillars with square cross section may display a re-entrant pinning regime as the density of the pillars is increased, a behaviour that is captured by neither of the aforementioned models. Numerically computed energy landscapes for the advancing meniscus allow us to explain the re-entrant behavior in terms of energy barriers between topologically different meniscus shapes. Our numerical approach is validated in wicking experiments using circular pillars where the re-entrant behaviour is absent for the material contact angle $\theta_0 = 47^\circ$ of our experiments.

1 Introduction

Wetting of physically structured and chemically heterogeneous solids is dominated by contact line pinning and contact angle hysteresis [1,2]. At the microscopic level, i.e. on the length scale set by the size of the heterogeneities, contact line pinning can be related to the dense spectrum of local energy minima and relative energy barriers that trap the interface of a partially wetting liquid in a metastable state [3]. The spatial distribution and shape of the surface heterogeneities determine the pinning forces and dissipation, which may display an orientational dependence. The resulting anisotropy of contact line pinning on regular microstructures gives rise to the strong faceting of static liquid shapes [4–6] or uni-directional spreading [7].

Under certain conditions a liquid drop placed on an uniform array of pillars is spontaneously drawn into the microstructures, where the liquid forms a film whose thickness equals the pillar height [8,9]. Conditions for spontaneous wicking are normally derived from global consideration of the interfacial energy neglecting the existence of metastable interfacial shapes. A typical 'wicking' behaviour, as illustrated in Fig. 1, can be intuitively explained by the gain of interfacial energy during formation of the liquid film. The energy gain grows with an increasing difference in surface energies between the dry and the wet state relative to the interfacial tension of the liquid. Hence, one can expect that the tendency to wick the topographies becomes stronger for smaller material contact angles θ_0.

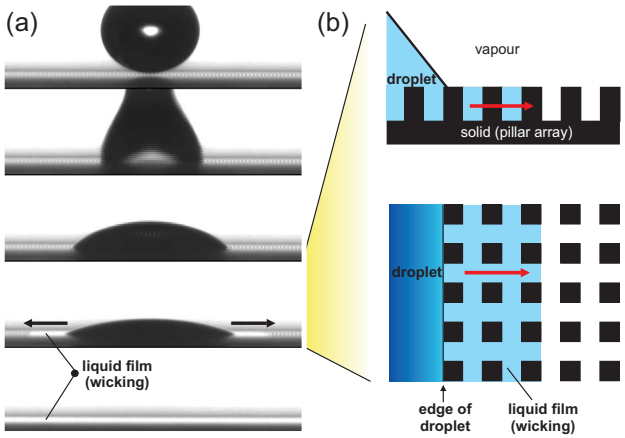

Fig. 1 (a): A time series showing the progression of wicking (spontaneous spreading of a liquid film in a pillar array). Two stages are observed: spreading of the droplet, followed by wicking which drains the liquid until only a film remains (see last frame). (b): Schematic of wicking in a pillar array viewed from side and above.

Accordingly, wicking should be favoured for substrates with a large Wenzel roughness factor $r = A/A_0$, given by the ratio of the total surface area A of the topography to the base area A_0. It is rather compelling to expect that substrates covered with dense high aspect ratio topographies strongly favour spontaneous wicking of a liquid film. Instead the results presented in this article show that this general conclusions is not always correct, as criteria for film formation or dewetting that are purely based on energy consideration may fail.

In order to quantify the influence of contact line pinning on the onset of spontaneous wicking we deployed a combined numerical and experimental investigation. Equilibrium shapes of

[a] *Department Dynamics of Complex Fluids, Max-Planck Institute for Dynamics and Self-Organization, Am Fassberg 17, D-37077 Göttingen, Germany.* [b] *Ian Wark Research Institute, University of South Australia, Mawson Lakes, South Australia 5095, Australia.* [c] *Uppsala University, Dept. of Engineering Sciences, Sweden.* [d] *Experimental Physics, Saarland University, 66123 Saarbrücken, Germany E-mail: ciro.semprebon@ds.mpg.de*

a straight liquid meniscus trapped in a square lattice of pillars are numerically computed to elucidate the interplay between pillar geometry, pillar density, material contact angle, and the stability of static meniscus morphologies. Additional insight into activation energies and the sensitivity of de-pinning of imperfections is gained using the method of energy landscapes. The results of our numerical investigations are described in stability diagrams illustrating the range of mechanically stable meniscus shapes. Our stability diagrams for pillars with circular and square cross section facilitate the comparison to wetting experiments on samples used in our experiments covering a wide range of aspect ratios and line fractions.

2 Wicking criteria

Most criteria for wicking of a liquid film into topographic substrates given in literature rely on energy considerations[9]. To illustrate this 'thermodynamic' approach, let us consider a periodic lattice of ideal pillars with vertical walls and flat top faces. Furthermore, assume that all vertical and all horizontal parts of the surfaces exhibit the same material contact angle θ_0, identical to the one measured on a plane unstructured reference substrate made of the same material. In presence of hysteresis the material angle is referred to the advancing or receding angle depending whether the contact line is respectively advancing or receding over the substrate. These conditions are typically satisfied where a surface is etched, embossed, or prepared using the multilayer photolithography method in this paper, see Fig. 2. The geometry of such a substrate is uniquely specified by the pillar height h,the width w, and the lattice constant d.

To further simplify the problem, assume a completely dry substrate and a large drop as the initial state, and a homogeneous film of thickness h filling the interstices of the pillars up to the level of the pillar tops as the final state. Now, for the given initial and final state it is straight forward to compute the difference of interfacial energy per base area. If the energy difference between the film and the completely dry state is smaller than zero, wicking of the liquid is possible but does not necessarily need to take place. The energy difference is negative for material contact angles, θ_0, below a critical contact angle, θ_c, given by[8,10,11]

$$\cos\theta_c = \frac{1-\phi}{r-\phi}, \tag{1}$$

where r is the Wenzel roughness factor, and ϕ the projected area fraction of the pillars, defined as the area of top faces to the total base area. If the energy difference between the final and the initial state is positive, the spreading of a continuous liquid film from a liquid reservoir at zero Laplace pressure is impossible. Strictly speaking, eqn. (1) can predict only conditions under which wicking or de-wicking can be safely excluded.

Besides this rather serious shortcoming, thermodynamic arguments do not permit any statement about the dynamics of wicking. Provided that there are two or more possible final states with a total interfacial energy lower than in the initial state, but still above the global thermodynamic minimum. If this is the case, details of the wicking dynamics are crucial to determine which final state will be attained[4]. Also the observation that, on regular topographic patterns, the front of a wicking film forms facets aligned with the lattice directions that cannot be explained by global thermodynamic arguments: the interfacial energy per projected area is a scalar quantity and hence the energy gain is the same irrespective of the direction of film propagation.

Alternatively the range of line fractions w/d and aspect ratios h/w that allow a static liquid meniscus to be estimated from a purely geometrical consideration. This criterion is based on the somewhat strong assumption of an essentially two-dimensional meniscus shape, i.e. the liquid film exhibits a homogeneous cross-section perpendicular to the movement of the film front. Furthermore, the criterion supposes that the liquid interface in the last row in contact with the liquid is straight and fully pinned to the top edge of the pillars, i.e., the pillar array is completely filled with liquid. It is clear that such interfacial morphology can be constructed whenever the material contact angle satisfies the inequality

$$\frac{h}{w} \leq \left(\frac{d}{w} - 1\right)\tan\theta_0 \tag{2}$$

The applicability and accuracy of the above criterion to predict wicking of a liquid film is limited. For material contact angles $\theta_0 > 45^\circ$ it is not clear whether the liquid interface of the meniscus will 'coalesce' in front of the pillars[12] so that the liquid completely surrounds the base of pillars situated at the liquid front. Especially for values of θ_0 slightly above 45°, a second mechanically stable morphology may be observed. In contrast to the coalesced meniscus morphology, the outermost contact line of the latter morphology is only partially located on the flat regions between the pillars.

3 Experimental methods

Fig. 2 shows the surface designs chosen for this study: a square lattice of pillars with either uniform square or circular cross section. The typical pillar width w, is 10μm and 20μm, while the lattice constant d is varied between 25μm and 160μm and the height h between 7μm and 60μm. The pillar arrays were prepared in SU8 photoresist using a standard UV-lithography process[2]. By preparing the pillars on top of a flat layer of hard-baked SU8 photoresist, we could ensure that

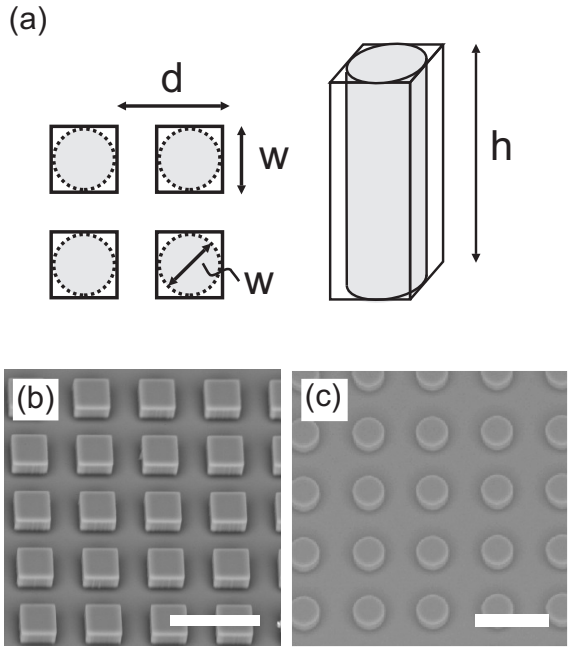

Fig. 2 Relevant dimensions, (a), and scanning electron microscopy images for the arrays of square (b) and cylindrical (c) pillars. Scale bars are 50μm.

the wettability of all surfaces in the pillar array were identical. After hard baking (200°C, 5 min), the samples were treated with sulphuric acid at high concentrations ($60-65\%$ vol) to make the SU8 more hydrophilic[13]. The static advancing contact angle was then carefully measured on flat (unstructured) regions of each sample using the sessile drop technique. On each sample, contact angles were extracted from between 12 and 15 images of droplets and averaged. If the contact angle was higher than our target value, the sample was treated again with a higher concentration of acid. If the contact angle was lower than our target value, the sample was baked again (200°C, 2 min) before subsequent acid treatment to achieve the correct contact angle. In the latter case, a higher acid concentration was generally required to achieve the target contact angle. Where the target material contact angle could not be achieved with sufficient precision on a given sample, the sample was discarded. It should be noted here that the acceptable contact angle window is very narrow, i.e., only a few degrees, due to the sensitivity of the wicking phenomena on the material contact angle (as discussed later). Once the desired contact angle was reached on the flat portion of the sample, water droplets were placed on the pillar arrays and observed to see whether wicking occurred.

4 Numerical methods

Throughout this work we performed numerical minimizations of the interfacial energy with the public domain software Surface Evolver[14]. In this software, the liquid-vapour interface of the film is represented by an irregular mesh of small triangles whose corners form the nodes of the mesh. Nodes which do not belong to the boundary of the liquid-vapour interface can take any position in three dimensional space. The particular geometry is taken into account by local constraints keeping the nodes forming the three phase contact line in contact to the substrate or the pillars. As it is uniquely defined by the closed contact line, the liquid-substrate interface is not explicitly modelled. Hence its area $A_{s\ell}$ can be obtained from a numerical integration of suitably chosen functions over the contact line[14]. Instead the area $A_{\ell v}$ of the liquid-vapour interface is simply the total area of all triangles of the mesh. The total interfacial energy

$$E = \gamma(A_{\ell v} - \cos\theta_0 A_{s\ell}) \ , \qquad (3)$$

is therefore a function of the Cartesian coordinates of all nodes, where γ denotes the liquid-vapor interfacial tension. The total interfacial energy eqn. (3) can be minimized using standard optimizations algorithms. Repeated re-meshing of the interface during the energy minimization guarantees a constant quality of the triangulation in terms of the uniformity of edge lengths and the distribution of angles between adjacent edges.

For the system considered here, effects of hydrostatic pressure are neglected as the vertical extension of the liquid interface in the film is limited by the height of the pillars. This height is only a few tens of microns, while the capillary length for water/air is roughly 2.7mm under normal conditions. In the wetting experiments, the liquid in the film is connected to a large feeding droplet. Hence, it is justified to regard the liquid-vapour interface a minimal surface in equilibrium, i.e., with vanishing mean curvature. In this case we do not need to globally constrain the liquid volume to a fixed value during the numerical minimizations.

We restrict our analysis to the case of a meniscus orientation parallel to the lattice directions, as observed in our experiments. If the line fraction of the pillars is high or, in other words, the gap width $d-w$ between two neighbours is small compared to their width w, only the first row of pillars affects the shape of the liquid front. If the spacing is large, also the next row of pillars behind the liquid front has a significant impact on the shape of the terminal part of the interface. In our numerical calculations we consider three pillar rows behind of the outermost contact line. In the range of line fractions considered the equilibrium shape of the meniscus is barely affected by increasing the number of rows to more than three. Due to the combined translational and mirror symmetry of the

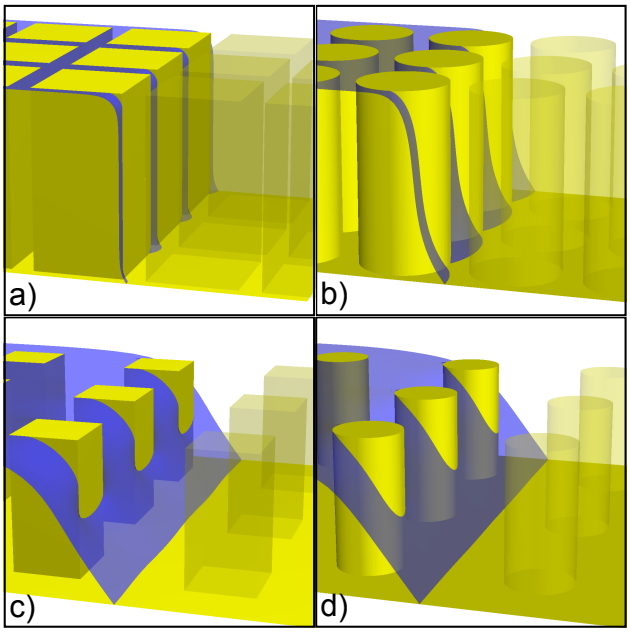

Fig. 3 Interfacial morphology of the liquid front between square (a,c) and circular pillars (b,d). The aspect ratio $h/w = 2$ and the material contact angle $\theta_0 = 52°$ is the same for all the plots. In (a) and (b), for a line fraction $w/d = 0.8$, the liquid interface is pinned, while in (c) and (d), for a line fraction $w/d = 0.4$, the meniscus is coalesced ahead of the pillars. Pillars ahead of the meniscus are drawn with higher transparency to allow a better visibility of the meniscus shape. Note how between circular pillars (b), the liquid protrusions are more extended than between square pillars (a), due to the strong pinning at the vertical edges.

liquid interface, only half of a unit stripe needs to be reproduced computed[15]. Examples of both pinned and coalesced interfacial morphologies are reported in Fig. 3 for surfaces patterned with both square and circular posts.

4.1 Energy landscape

Besides mechanically stable configurations of the liquid interface, we determine the energy landscape of transient meniscus shapes during an advancement or retraction of the film. The fundamental idea behind the method of energy landscapes is to compute local mechanical equilibrium under a subsidiary constraint that fixes a quantity x related to the global shape of the interface to a certain value ξ. The corresponding energy landscape $E^*(\xi)$ is then given by the value of the total energy of the system in a local energy minimum on the subset of states that satisfy the constraint $x = \xi$. If the system is now released from this additional constraint, it will relax into one of the proximal local minima of the energy landscape which represent the stable states of the system. The 'mountain pass lemma' guarantees the existence of an unstable equilibrium state (saddle point) between two local minima of the energy landscape*. The analysis of the values $E^*(\xi)$ between two local minima at $\xi = x_1$ and $\xi = x_2$ gives valuable insight into the activation energy related to the transitions between them. A proper choice of the constrained quantity x providing the coordinate is essential to unfold the energy landscape. The coordinate x could be, e.g. the centre of mass of a liquid droplet[16–19] or any other quantity that smoothly changes between the different local energy minima.

To study the energy landscape of the film meniscus in contact to the surface topographies, the interfacial energy of the liquid-vapour $E_{\ell v}$ interface is minimized under the constraint of a fixed liquid-substrate area $A_{s\ell}$. This choice allows us to keep the condition of a liquid interface of zero mean curvature. Owing to the periodicity of the topographic pattern, the energy energy landscape $E^*_{\ell v}(A_{s\ell})$ is periodic in $A_{s\ell}$ with a period A_0 given by the area of the substrate in contact to a complete film per unit cell. The energy landscape $E^*(A_{s\ell})$ of the total interfacial energy is then obtained by adding the missing contribution of the wet substrate. Since we have chosen $A_{s\ell}$ as the constrained quantity, we simply have

$$E^*(A_{s\ell}) = E^*_{\ell v}(A_{s\ell}) - \gamma \cos\theta_0 \, A_{s\ell} \tag{4}$$

and we are able to compute the energy landscape of the meniscus for arbitrary contact angles θ_0 a posteriori. Different values of the material contact angle θ_0 result in a different global tilts of the energy landscape $E^*(A_{s\ell})$. Interfacial shapes that correspond to a horizontal point of the energy landscape, i.e. which satisfy

$$\frac{\partial E^*}{\partial A_{s\ell}} = 0 \tag{5}$$

are local extrema of the total interfacial energy (3). According to the condition of Young-Dupré, any of the constraint energy minima must exhibit a constant contact angle on the smooth parts of the surface which is identical to the value of θ_0 specified in eqn. (4). Hence, we can conclude that every interfacial configuration corresponding to an unconstrained minimum of the interfacial energy forms a contact angle

$$\theta = \arccos\left(\frac{1}{\gamma}\frac{\partial E^*}{\partial A_{s\ell}}\right) \tag{6}$$

Further information about the stability of the extremal can be inferred from the energy landscape $E^*(A_{s\ell})$: Any mechanically stable shape must correspond to a minimum of $E^*(A_{s\ell})$ and, hence, has to satisfy the additional condition

$$\frac{\partial^2 E^*}{\partial A_{s\ell}^2} > 0\,, \tag{7}$$

i.e. the energy landscape has to be a convex upwards function.

* In the context of reaction kinetics this state is termed the 'activated complex'.

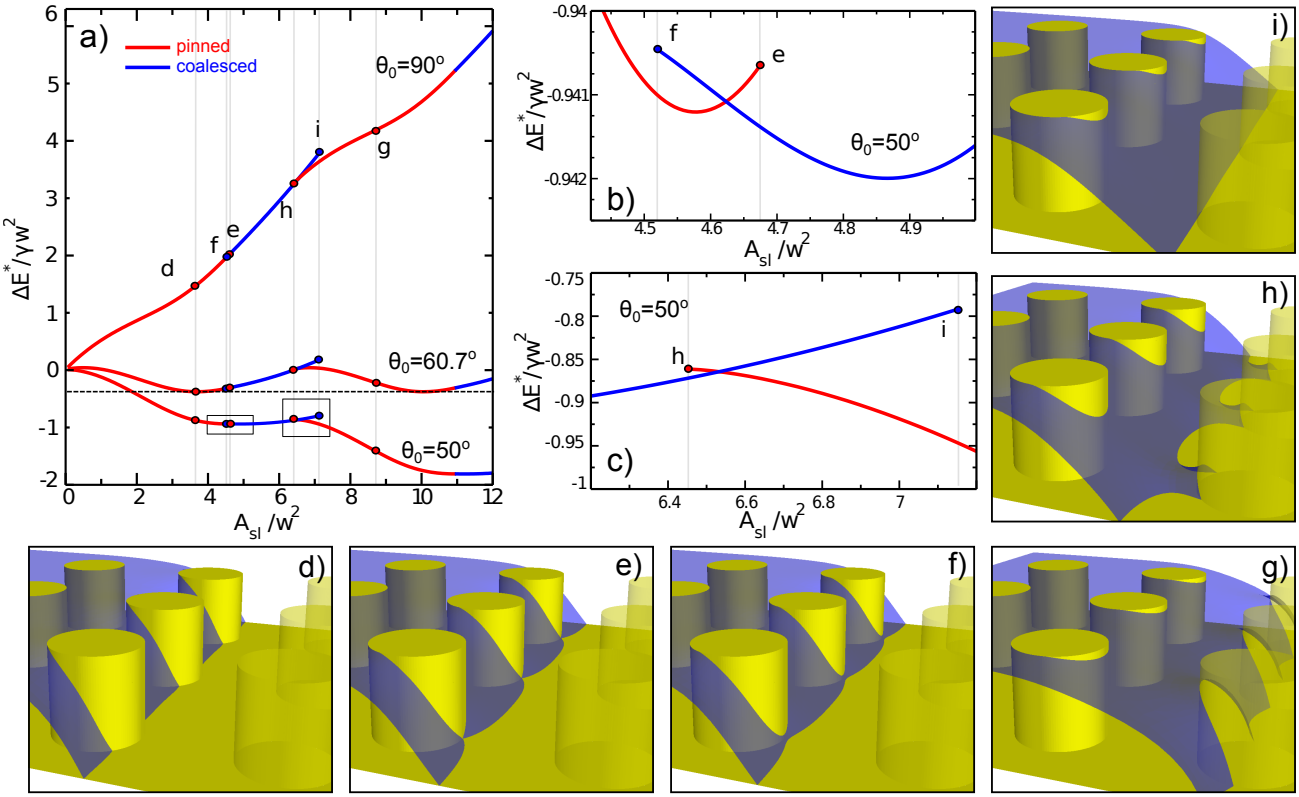

Fig. 4 a) Energy landscape $E^*_{\ell v}(A_{s\ell})$ of the row by row wicking process between circular pillars ($w/d = 0.5$ and $h/w = 1$). Red and blue lines refer to the pinned and coalesced branches, respectively. The local slopes are related to the contact angle θ of the liquid interface through eqn. (6). Letters (d-i) refer to the morphologies in the corresponding panels. See main text for details. The landscape $E^*(A_{s\ell})$ is reproduced for the material angle of the thermodynamic criterion $\theta_0 = 60.7°$, eqn. (1), and $\theta_0 = 50°$, adopted for the stability diagram in Fig. 5. b) Magnification of the energy landscape in proximity of the coalescence and de-coalescence instability. c) Magnification in proximity of the touching and pinch-off instabilities.

The complete set of branches of $E^*_{\ell v}(A_{s\ell})$ for given control parameter, in our case the aspect ratio h/w and line fraction w/d of the pillars, permits to construct a full stability diagram for any value of θ_0. An alternative choice of the constraint quantity is the total liquid volume of the film[20]. In that case the material angle on the substrate is preserved, but a finite Laplace pressure and a non-zero mean curvature of the liquid interface is introduced.

5 Results and Discussion

5.1 Analysis of the energy landscape

In the generic case considered in our numerical energy minimizations, matching the typical values of h/w and w/d of the experiments, the energy landscape $E^*(A_{s\ell})$ of the liquid meniscus forms two separate branches. An example for the energy landscape for circular pillars with line fraction $w/d = 0.5$ and aspect ration h/w is displayed in Fig. 4 for different values of the material contact angle θ_0. The meniscus morphologies corresponding to the black and red branches differ in the topology of the liquid-vapour interface close to the contact line. Both morphologies can be distinguished by the shape of the contact line segments located in the bottom plane of the substrate. The liquid-vapor interface of the 'coalesced' morphology is located entirely on the bottom of the substrate in front of the outermost row of wet pillars. For the 'non-coalesced' morphology, the contact line on the bottom of the substrate forms two disconnected segments. The remaining segments of the contact line make excursions onto the side walls of the pillars in the outermost wetted row. Renderings of the two respective morphologies are shown also in Fig. 3.

Each of the two morphologies mentioned above is described by a branch of the constraint interfacial energy $E^*_{\ell v}(i, A_{s\ell})$ with $i \in \{c, n\}$ for the coalesced and non-coalesced shapes, respectively. The plots in Fig. 4 show the two branches for a typical substrate geometry. From the definition, it is clear that the domains of the two branches are overlapping in a certain range

of $A_{s\ell}$. It is apparent from Fig. 4 that both branches display regions with either positive and negative convexity. As mentioned in the previous subsection, a point on a branch represents either a stable or an unstable equilibrium shape for the particular value of the material contact angle given by eqn. (6). As expected, the non-coalesced branch in point d) in the plot Fig. 4 a) which is excelled by the commont tangent construction becomes a horizontal point of the branch if we set θ_0 to the material contact angle eqn. (1) of the theromdynamic wicking condition.

Imagine that we could change the contact angle θ_0 or the geometry of the substrate fixed by h/w and w/d in a continuous way while following the set of equilibrium configurations corresponding to the horizontal points on the branches $E^*(\mathrm{c}, A_{s\ell})$ and $E^*(\mathrm{n}, A_{s\ell})$. During such a continuous change of the control parameters we would be able to encounter several types of interfacial instabilities, because a particular meniscus morphology has to decay into a different morphology when reaching one of the two end points terminating the respective branch. These endpoints could be related to a topology change of the interface, as for the configurations shown in Fig. 4 e) and f), where respectively a coalescence and de-coalescence of the interface in front of the pillars is observed. Alternatively the liquid interface shown in Fig. 4 h) at the end of the coalesced branch for larger values of $A_{s\ell}$ is touching the base of the row of pillars in front of the film and is related to an instability that raises the interface.

Yet another type of instability occurs when an inflection point is traversed and the convexity criterion eqn. (7) of the branch becomes violated. Inspection of Fig. 4 c) shows that the meniscus morphology corresponding to this case does not display any particular feature apart from the soft mode that drives the meniscus to the end point d) at small values of $A_{s\ell}$. The interfacial shape in Fig. 4 d), however, is close to the final 'pinch-off' instability at the end of the non-coalesced branch, has formed liquid 'necks' and adheres only in a small area on the backside of the foremost row of pillars. The final break-up of these necks during a further decrease of $A_{s\ell}$ resembles the Rayleigh Plateau instability of free-standing cylindrical interface. It is reasonable to imagine that during the final pinch off a small deposit of liquid can remain attached between the substrate and the back of the pillars, similarly as it was observed during the receding process of the contact line on a super amphiphobic substrate[21,22].

5.2 Stability diagrams

In the previous subsection we demonstrated how the mechanical stability of the two principal meniscus shapes can be inferred from the method of energy landscapes. For the sake of comparability, we chose the same material contact angle $\theta_0 = 50^\circ$ in the stability diagram for pillars with circular and square cross section in Fig. 5 a) and b), respectively. Regions of the control parameter h/w and w/d where a particular meniscus shape exists and is mechanically stable are indicated with Roman numerals in the two stability diagrams, with boundaries denoted by the same lower case letters utilized in Fig. 4.

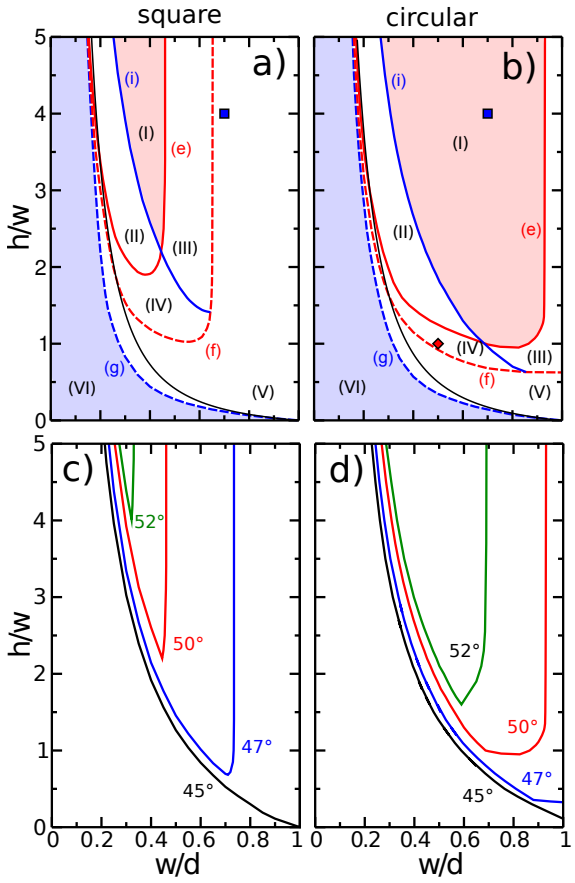

Fig. 5 Stability diagrams for pinned and coalesced morphologies on both square (a) and circular (b) pillars with material contact angle $\theta_0 = 50^\circ$. Instability lines are indicated by capital letters, stability regions by Roman numbers. Refer to the main text for details. The red diamond is referred to the geometry of the energy landscape in Fig. 4. The blue squares are referred to Fig. 8 for the stability of the the coalesced meniscus. c,d) Wicking regions for square and circular pillars respectively for material angles of $\theta_0 = 45^\circ$ (black), $\theta_0 = 47^\circ$ (blue), $\theta_0 = 50^\circ$ (red) and $\theta_0 = 52^\circ$ (green).

In both diagrams we find a boundary line (e) where the interface of non-coalesced morphology coalesces in front of the outermost row of pillars. Furthermore, we have a boundary line (i) where the three phase contact line of the coalesced morphology touches the outermost row of dry pillars, and a line (f) where the interface of the coalesced morphology decoalesces in the front of a the outermost row of pillars. The boundary line (h) indicates the pinch-off instability. In addi-

tion to lines indicating instabilities, we plot the function

$$\frac{h}{w} = \frac{1-\phi}{4\phi}\left(\frac{1}{\cos\theta_0} - 1\right) \quad (8)$$

where the liquid film and the completely dry state exhibit the same energy is plotted as a solid black line in Fig. 5 a) and b). The expression eqn. (8) is derived from eqn. (1) and is valid for pillars with regular polygonal shape having n sides and inscribed by a circle of radius $w/2$. In this case the roughness factor can be simply expressed in terms of the density of pillars $r = 1 + \frac{h}{w} 4\phi$, where $\phi = \frac{w^2}{d^2}\frac{n\tan(\pi/n)}{4}$. In particular we have $\phi = \frac{w^2}{d^2}$ for square and $\phi = \frac{\pi}{4}\frac{w^2}{d^2}$ for circular pillars, respectively.

The set of stability lines partitions the plane of control parameters w/d and h/w into several regions. In each of these regions denoted by capital Roman numerals certain meniscus shapes exist and are mechanically stable. In the red shaded region (I) of Fig. 5 a) and b), neither the coalesced nor the non-coalesced meniscus morphology is stable or exists. In addition, the film state has a lower energy as compared to the dry state. In region (II), however, the coalesced morphology is stable while the non-coalesced morphology is unstable or does not exist. The opposite case, i.e. with the coalesced meniscus shape being stable and the non-coalesced being unstable or non-existing is found in region (III). Both the coalesced and the non-coalesced morphology are stable in region (IV) while in region (VI), shown as a blue shaded region in Fig. 5 a) and b), we again face the situations that neither the coalesced nor the non-coalesced morphology are stable or exist. In region (VI) the dry state represents the state of lower interfacial energy when compared to the film state in contrast to region (I).

The stability boundaries of the coalescence instability (e) and the de-coalescence instability (f) become asymptotically vertical as the line fraction w/d of the pillars increased towards one in both stability diagrams Fig. 5. In other words, the criterion for an interfacial instability corresponding to line (e) and (f) is virtually independent on h/w for pillars with a sufficiently high aspect ratio.

The asymptotic independence of the coalescence line (e) on h/w can be readily explained by the observation that the shape of the interface close to the bottom of the substrate is barely affected by the region close to the pillar tops and, hence, must become independent on h/w for high values. Due to this screening, we observe a flat interface spanning between the side walls of the pillars apart from the regions in the vicinity of the top or bottom of the pillars. This feature is clearly visible for the non-coalesced meniscus shape displayed in Fig. 3 a).

The coalescence line (e) which is related to a topological transition of the interface if the two tips of the liquid in the wedge-shaped region formed by the side wall and the bottom of the substrate touch. The de-coalescence line (f), however, is linked to the appearance of a soft mode as it was discussed in the previous subsection on the energy landscape. A displacement of the contact line is related to only small changes of the interfacial energy. The resulting restoring force driving the contact line away or toward the pillars will become zero for infinitely high pillars.

For square pillars such geometry is close to the soft mode instability to a non coalesced morphology, while for circular pillars it represents a stable coalesced meniscus. Clearly the soft mode is accompanied by a variation of the wet area of the substrate, $A_{s\ell}$. Hence, it must be related to a horizontal region on the branch $E^*(c, A_{s\ell})$ of the energy landscape. This 'straight' region close to the left end point of the coalesced branch is clearly visible in the energy landscape plotted in Fig. 4 for $\theta = 50°$. The corresponding point in Fig. 5 b) defined by the aspect ratio h/w and line fraction w/d of Fig. 4 is indicated by the diamond shaped symbol. While approaching the transition line (f) the slight tilt of the energy landscape towards higher values of $A_{s\ell}$ will disappear. The instability line (i) in Fig. 5 a) and b) corresponds to the right endpoint of the coalesced branch and is linked to the touching next row of pillars ahead. Consequently, the instability line (i) must terminate on (f) once the touching condition is already met for values $A_{s\ell}$ in the region of the soft mode.

The appearance of a soft mode as the underlying mechanism for the de-coalescence instability in the limit of high aspect ratio pillars also explains the qualitative difference of line (f) between square and circular pillars for the particular value $\theta_0 = 50°$ chosen here. For square pillars, the instability line (f) exhibits a vertical asymptote approaching $w/d = 0.655$ from below. For the case of circular pillars, however, the line (f) approaches the value $w/d = 1$ at a finite aspect ratio $h/w = 0.65$. Further considerations based on energy balance allowed us to derive an exact expression $f(\theta_0)$ for the line fraction w/d where the line (f) becomes asymptotically vertical. A vertical asymptote for (f) is missing whenever $f(\theta_0) > 1$. Details of the derivation and the particular form of $f(\theta_0)$ for circular and square pillars are outlined in the appendix.

5.3 Comparison to experimental results

It is reasonable to assume that spontaneous wicking can be observed in experiments on samples with pillars of aspect ratios h/w and line fractions w/d that fall into the respective regions (I) of the stability diagrams Fig. 5 a) and b). In this region of control parameters h/w and w/d, no stable meniscus shapes are found while the film state has a lower interfacial energy than the completely dry state.

From the construction of the energy landscapes it is clear that the shape of region (I) varies with the material contact angle θ_0. The plots in Fig. 5 c) and d) illustrate the sensitivity of region (I) with respect to small variations of θ_0 in the narrow range between 45° and 60°. Comparing the shape of the

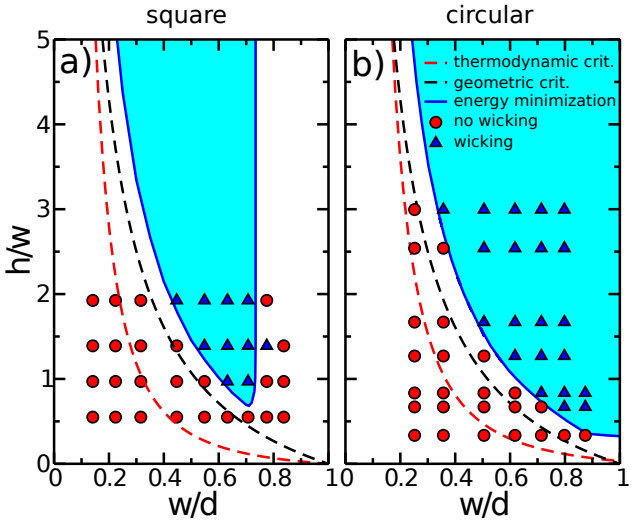

Fig. 6 Comparison of experimental data for square and circular pillars with the thermodynamic criterion (red dashed line) eqn. (8) and the straight wedge approximation (blue dashed line) eqn. (2), for the onset of wicking. Triangle and circle symbols represent experiments where wicking and non-wicking was observed, respectively.

boundary curves for $\theta_0 = 47°$ and $50°$ shows that also the coalescence line (e) may lack a vertical asymptote for large line fractions. For values slightly above $\theta_0 = 45°$ the two pointed parts of the liquid meniscus protruding into the wedge formed by the bottom substrate and side walls will always coalesce. A comparison of the boundary lines at $\theta_0 = 45°$ in Fig. 5 c) and d) shows that the tendency to coalescence is less pronounced for square pillars owing to the sharp vertical edges impeding coalescence of the liquid tips.

The main results of our experiments are summarized in the diagrams shown Fig. 6. Samples that showed wicking are displayed by a triangular symbol at their respective values of line fraction w/d and aspect ratio h/w. Correspondingly, circular symbols represent samples where no wicking was observed. The material contact angle as measured on a plane part of the substrate is $\theta_0 = (47 \pm 1)°$ throughout all experiments.

As an example for circular pillars with aspect ratio $h/w = 0.82$, wicking was observed only for line fractions $w/d \sim 0.3$ larger than the value predicted by the thermodynamic criterion eqn. (8). The difference between the experimentally observed transition between wicking and non-wicking corresponds to a decrease in the lattice spacing, d, from 50μm to 30μm for pillars of width $w = 20\mu$m, representing a significant difference in the surface structure. This difference is reduced for taller circular pillars but is still evident until at least $h/w \approx 3$.

Even more striking are the results for square pillars, where a transition from non-wicking to wicking and back to non-wicking is observed in our experiments during an increase of w/d at fixed h/w. Consider, for example, square pillars with aspect ratio $h/w = 1$. While increasing w/d, wicking first occurs at $w/d \approx 0.59$ (compared with the value 0.33 predicted by eqn. (2), and persists only until $w/d \approx 0.74$. Increasing the height of the square pillars, the first transition is shifted to lower values of the line fraction w/d, e.g. $w/d \approx 0.38$ for $h/w = 2$. The point of the transition from spontaneous wicking back to non-wicking instead remains unchanged, within the uncertainty of our measurements. The straight wedge approximation given by eqn. (2) predicts values of the line fraction w/d for the onset of wicking closer to our experimental results, but does not capture the re-entrant behaviour observed for square pillars.

A striking coincidence between the experimental results and the numerically computed region (I) is found for the material contact angle $\theta_0 = 47°$. Apart from a single experimental data point for square pillars, the full boundary line is reproduced by our numerical calculations, including the re-entrant transition from wicking to non-wicking at high line fractions in the case of square pillars.

5.4 Discussion

The method of energy landscape employed to infer the stability of the liquid morphologies can be applied in a variety of problems. Applications range from conformational transitions and pore formation in lipid membranes[23,24] to droplets moving over wettability patterns[25]. In this context the analysis of the energy landscape is a first step toward understanding dynamic phenomena in complex geometries. Consider for example wicking of a viscous liquid, such that inertial effects become negligible: it is plausible that the dynamic contact angle will follow the sequence of unstable morphologies described by the energy landscape. In this case its global tilt will be related to the apparent dynamic contact angle of the meniscus through eqn. (6). Hence it would be possible to use this information to calculate the dissipation rate through a suitable model[1] for dynamic wetting. Such assumption could be verified by implementing an effective law for the motion of the contact line, where the velocity is given for example by a power law of the dynamic angles. A similar approach has been recently adopted to investigate the onset of motion of drops driven by a body force[26].

Information on the dissipation rate, related to the details of the geometry of the system, could be important to include dynamic effects in the stability diagrams presented here. Consider, for example, region (III) in Fig. 5. If the energy released after touching the next row of pillars is not dissipated quickly enough, it might be sufficient to overcome the small energy barrier required to coalesce ahead of the posts. In this case the spreading process could be dynamically self-sustained beyond the region where spontaneous spreading is predicted.

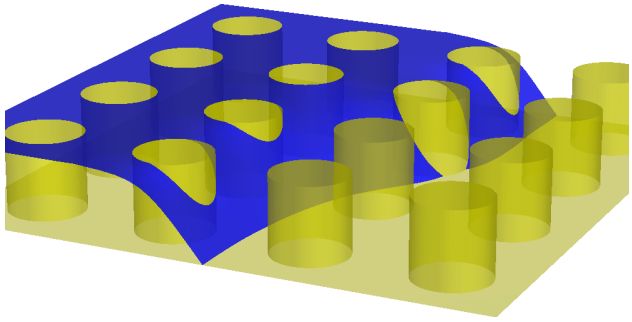

Fig. 7 Example of numerically minimized interface with a kink. If a sufficient number of kinks is created, kink propagation can be regarded as an additional wicking mechanism.

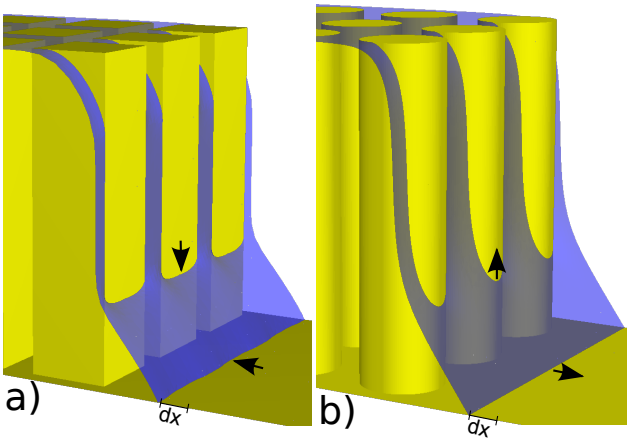

Fig. 8 Meniscus shape close to the soft mode prior to decoalescence.

Our analysis is based on the assumption that the front of the liquid film is aligned parallel with the rows of pillars. Consequently, all interfacial instabilities predicted using the method of energy landscapes were derived from the same assumption. Experimental observations, however, evidenced another possible mechanism, which is related to the nucleation and lateral propagation of a kink in the liquid front[4]. As the nucleation of a kink can be triggered by surface defects, in the presence of a sufficient number of them, the kink propagation could represent an additional wicking mechanism. In Fig. 7 we report a numerical example of such a kink in the liquid meniscus between circular pillars.

Kink propagation can also play an important role in the dynamic process and has been also investigated in the context of superhydrophobicity[27] and its breakdown[28,29]. For our scope however a more complete analysis of the conditions for the kink propagation is rather involved, because the number of topologies that must be accounted for, rapidly increases with the number of pillars in proximity of the kink. Wicking criteria could also be significantly different when considering different pillar geometries, i.e. triangular[30] or polygonal[20]. Directional wicking can instead occur in presence of slanted pillars[31].

6 Conclusion

In this paper we experimentally investigated the onset of wicking of a liquid film on a regular pattern of square and circular pillars. Numerical energy minimizations allowed us to calculate the energy landscape of the process and determine the stability diagram. In particular, spontaneous wicking is predicted in regions where both the detected liquid morphologies, pinned and coalesced, do not present energy minima in the landscape. If at least one of the two exhibits a local minimum, it is necessary to overcome an energy barrier, also determined. As instabilities can occur both while increasing and decreasing the total wet area, we could determine also the region where spontaneous de-wicking of an already present liquid film should occur. The region where wicking is observed is often characterized by a re-entrant behaviour, which cannot be captured by thermodynamic arguments or by a simplified model based on a straight wedge ahead of the pillars.

Acknowledgements

Part of this work was carried out at the South Australian node of the Australian National Fabrication Facility. The authors thank Dipankar Chugh and Frederik Kriel for their assistance in preparing and characterizing micropillar arrays. Funding from DFG within the Grant no. HE 2016/14-2 Piko and from the Australian Research Council are acknowledged.

Appendix

The variation of the interfacial energy E of the meniscus per period d can be written as the sum of the energy contribution E_{vert} related to the wet side walls of the first row of pillars and the interface spanning between the pillars, the interfacial energy of the liquid-solid contact on the bottom, $E_{s\ell}$, and the slated liquid-vapour interface $E_{\ell v}$. A typical interfacial configuration is illustrated in Fig.8.

A soft mode occurs if the total interfacial energy E does not change in linear order under a displacement of the contact line by a length dx:

$$\mathrm{d}E = \mathrm{d}E_{\mathrm{vert}} + \mathrm{d}E_{\mathrm{sl}} + \mathrm{d}E_{\ell v} = 0\,. \qquad (9)$$

The variation of the interfacial energy of the vertical walls of the pillars and the liquid meniscus filling the interstices becomes

$$\mathrm{d}E_{\mathrm{vert}} = \left[\gamma(d-w) + (\gamma_{\ell v} - \gamma_{\mathrm{sl}})w\right]\tan\theta_0 \mathrm{d}x \qquad (10)$$

while the variation of the interfacial energy related to the bottom part of the substrate can be written as

$$\mathrm{d}E_{\mathrm{sl}} = (\gamma_{\mathrm{vs}} - \gamma_{\mathrm{s}\ell})\mathrm{d}x\,. \tag{11}$$

Finally, the variation of the interfacial energy of the slanted liquid-vapor interface is given by

$$\mathrm{d}E_{\ell\mathrm{v}} = \frac{\gamma}{\cos\theta_0}\mathrm{d}x\,. \tag{12}$$

Using the condition of Young-Dupré $\gamma\cos\theta_0 = \gamma_{\mathrm{sv}} - \gamma_{\mathrm{sl}}$ in eqns. (10) and (11), we finally arrive at the condition

$$w/d = f_{\mathrm{s}}(\theta_0) = \frac{\sin\theta_0 - 1}{\cos\theta_0 - 1} \tag{13}$$

for the occurrence of the soft mode. It is straight forward to see that $\mathrm{d}E < 0$ for $\mathrm{d}x < 0$ whenever $w/d > f_{\mathrm{s}}(\theta_0)$, i.e. at line fractions above this values the meniscus spontaneously decoalesces.

In case of circular pillars the energy contribution $\mathrm{d}E_{\mathrm{vert}}$ reads

$$\mathrm{d}E_{\mathrm{vert}} = \left[(d - w\sin\theta_0) + w\theta_0\cos\theta_0\right]\tan\theta_0\mathrm{d}x \tag{14}$$

and we obtain

$$f(\theta_0) = \frac{\sin\theta_0 - 1}{\theta_0\cos\theta_0 - \sin\theta_0} \tag{15}$$

Note that for circular pillars, we have $f(\theta_0) > 1$ already for $\theta_0 \gtrsim 51.32^\circ$, while $f_{\mathrm{c}}(50^\circ) = 1.14$, consistent with the absence of vertical asymptotes in for the de-coalescence instability in the stability diagram in Fig. 5.

References

1 D. Bonn, J. Eggers, J. Indekeu, J. Meunier, and E. Rolley. *Rev. Mod. Phys.*, 2009, **81**, 739.
2 P.S.H. Forsberg, C. Priest, M. Brinkmann, R. Sedev, and John Ralston. *Langmuir* 2010, **26**, 860.
3 R. Blossey. *Nature Materials*, 2003, **2**, 301.
4 L. Courbin, E. Denieul, E. Dressaire, M. Roper, A. Ajdari, and H.A. Stone. *Nature materials*, 2007, **6**, 661.
5 L. Courbin, J.C. Bird, M. Reyssat, and H. A. Stone. J. Phys.: Condens. Matter 21 , 2009, **21**, 464127.
6 M.L. Blow and J.M. Yeomans. *Phil. Trans. R. Soc. A* 2011, **369**, 2519.
7 K. H. Chu, R. Xiao, and E. N. Wang. *Nature Materials*, 2010, **9**, 413.
8 J. Bico, U Thiele, and D. Quéré. *Coll. Surf. A*, 2002, **206** 41.
9 David Quéré. *Ann. Rev. Material Research*, 2008, **38**, 71.
10 C. Ishino, K. Okumura, and D. Quéré. *EPL*, 2004, **68**, 419.
11 C. Ishino, M. Reyssat, E. Reyssat, K. Okumura, and D. Quéré. *EPL*, 2007, **79**, 56005.
12 R. Seemann, M. Brinkmann, S. Herminghaus, K. Khare, B.M. Law, S. McBride, K. Kostourou, E. Gurevich, S. Bommer, C. Herrmann, and D. Michler. *J. Phys. Condens. Matter* 2011, **23**, 184108.
13 C. Priest, P.S.H. Forsberg, R. Sedev, and J. Ralston. *Microsystem Technologies*, 2011, **18**, 167.
14 K. Brakke. *Phil. Trans. Royal Soc. London, Ser. A*, 1996 bf 354, 2143-2157.
15 C. Semprebon, S. Herminghaus and M. Brinkmann. *Soft Matter*, 2012, **8**, 6301.
16 M. Brinkmann and R. Lipowsky. *J. App. Phys.*, 2002, **92**, 4296.
17 H. B. Eral, J. de Ruiter, R. de Ruiter, J. M. Oh, C. Semprebon, M. Brinkmann, and F. Mugele. *Soft Matter*, 2001, **7**, 5138.
18 R. de Ruiter, J. de Ruiter, H. B. Eral, C. Semprebon, M. Brinkmann, and F. Mugele. *Langmuir*, 2012, **28**, 13300-6.
19 D. Ferraro, C. Semprebon, T. Tóth, E. Locatelli, M. Pierno, G. Mistura, and M. Brinkmann, *Langmuir*, 2012 **28**, 13919-23.
20 R.J. Vrancken, M.L. Blow, H. Kusumaatmaja, Ko Hermans, An M. Prenen, C. W. M. Bastiaansen, D.J. Broer, and J.M. Yeomans. *Soft Matter*, 2013.
21 R. Dufour, M. Harnois, V. Thomy, R. Boukherroub, and V. Senez. *Soft Matter*, 2011, **7**, 19.
22 R. Dufour, P. Brunet, M. Harnois, R. Boukherroub, V. Thomy, and V. Senez. *Small* , 2012, **8** 1229.
23 H.G. Döbereiner and U. Seifert. *EPL* , 1996, **36**, 325.
24 K. Katsov, M. Müller, and M. Schick. *Biophysical Journal*, 2006, **90**, 915.
25 D.Herde, U. Thiele, S. Herminghaus and M. Brinkmann, *EPL*, 2012, **100**, 16002.
26 C. Semprebon and M. Brinkmann. *Soft matter*, 2014 **10** 3325
27 A. Gauthier, M. Rivetti, J. tesseire, and E. Barthel. *PRL*, 2013, **110**, 046101.
28 M. Sbragaglia, A. Peters, C. Pirat, B. Borkent, R. Lammertink, M. Wessling, and D. Lohse. *PRL*, 2007, **99**, 156001.
29 C. Pirat, M. Sbragaglia, M. Peters, B. M. Borkent, R.G.H Lammertink, M. Wessling, and D. Lohse. *EPL* , 2008, **81**, 66002.
30 M.L. Blow, H. Kusumaatmaja, and J.M. Yeomans. J. Phys.: Condens. Matter 21 , 2009, **21**, 464125.
31 A. Cavalli, M.L. Blow, and Julia M. Yeomans. *Soft Matter*, 2013, **9**, 6862.